ADVANCED MATERIALS TECHNOLOGIES
www.advmattechnol.d

Direct Ink Writing of Wearable Thermoresponsive Supercapacitors with rGO/CNT Composite Electrodes

*Yizhou Jiang, Meng Cheng, Reza Shahbazian-Yassar, and Yayue Pan**

Developing intelligent wearable energy storage devices that can endure harsh conditions is of interest for emerging applications in next-generation electronics. Despite recent success in exploring functional materials for sophisticated self-adaptivity in energy storage devices, it remains challenging to obtain both high reliability and superior performance. Herein, a novel method for fabricating micropatterned wearable thermoresponsive supercapacitors via direct ink writing (DIW) technique is reported. Thermal runaway of typical electrochemical storage devices with high power delivery capability can cause serious safety problems. The proposed temperature-dependent structure works as self-protection against the common thermal runaway issues of electrochemical energy storage devices. Such construction provides an automatic adjustment as high as 8 F g^{-1} in specific capacitance, resulting in an overall heat reduction by up to 40%. The printing resolution of the electrodes (175 µm) is among the best in recently reported planar carbon-based energy storage devices by DIW technique. Manufacturing-related parameters such as time-dependent printing speed and curing temperature are also investigated to fabricate this integrated design with varied materials and accuracy. This strategy shows tremendous promise for future intelligent energy storage devices.

Carbon-based supercapacitors (SCs) are of significant interest in wearable electronics, sensing, energy harvesting, and medical applications.[1–4] They are considered as the next-generation energy storage devices, with unique electrical and mechanical properties. The intrinsic characteristics of porous carbon, including high specific surface area, uniform pore size distribution, and excellent conductivity play an essential role in electrochemical performance. Furthermore, extensive efforts have been made recently on the design and manufacturing of flexible SCs, which can maintain their electrochemical performance under deforming (bending, stretching, or twisting). Despite these advances, they lack the self-protection against harsh conditions, to further realize the potential for intelligent energy storage devices. For SCs, one of the most common safety issues is the thermal runaway, which is caused by the considerable heat generated during rapid charging and discharging.[5,6]

Y. Jiang, M. Cheng, Prof. R. Shahbazian-Yassar, Prof. Y. Pan
Department of Mechanical and Industrial Engineering
University of Illinois at Chicago
Chicago, IL 60607, USA
E-mail: yayuepan@uic.edu

The ORCID identification number(s) for the author(s) of this article can be found under https://doi.org/10.1002/admt.201900691.

DOI: 10.1002/admt.201900691

When SCs are used in harsh conditions, like the extreme weather, or with electronic components that generate significant heat locally, the thermal runaway issue is even more frequent or severe. Thermal runaway damages to the product, such as explosion and fire, have been widely reported and remain a significant challenge in SCs applications. Some electrode/electrolyte materials may also produce harmful compound by-product and bring new environmental issues. For example, under an overheated condition caused by the thermal runaway, the reaction of the lithium-ion battery electrolyte with the material of the unprotected positive electrode results in the formation of toxic fluoro-organic compounds.[7] Conventional solutions to address the thermal runaway issues in SCs are using alternative electrode or electrolyte materials or adding heat sinks. However, alternative materials, including solid-state or polymer gel electrolytes, show low ionic conductivity.[8] This method provides an immutable slow charging/discharging rate under various thermal conditions. The addition of heat sink makes the device bulky and impossible for some applications that require flexibility and compact. Besides, almost all these approaches compromised the energy performance of SCs, which is degraded by the static charge–discharge rate under the various thermal circumstances. To overcome these shortcomings, herein, we report a novel temperature-dependent SCs structure that works as self-protection against the thermal runaway issues with a powerful and efficient thermoresponsive mechanism, by self-adjusting the charge–discharge rate according to environmental temperature. Besides, this novel thermoresponsive SCs structure not only addresses the thermal runaway but also functionalizes the smart thermal sensing in wearable electronics applications.[9–16] Recently, due to the extension to the capabilities of medical monitoring, the thermoresponsive energy storage devices can be integrated into the routine care of patients with chronic diseases, providing an accurate tracking and a reliable drug delivery process for the healthcare management.[17–19]

To realize the temperature-dependent structure, we propose to integrate shape memory materials in SCs design. Shape memory alloys (SMAs) can endure reversible phase transitions stimulated by temperature or humidity. Such mechanical property they exhibited is namely pseudoelasticity. Numerous applications of SMAs include valves in piping systems,

packaging devices, and biomedical materials.[20–22] Although many studies of shape memory polymers (SMPs) have been reported, most of them are limited to one-way shape memory behavior, and the cycling time is usually minimal.[23–27] Compared with SMPs, SMAs shows higher stability and minor long-term fatigue, which enables a more reliable SC construction. Hence, in this study, SMA is investigated to allow for the thermoresponsive and self-protection functionality of SCs.

Reduced graphene oxide (rGO) and carbon nanotube (CNT) are commonly used as the electrode materials of high-performance SCs, mainly due to their high electrical conductivity and large specific surface area.[28,29] Interestingly, recent studies have reported the benefits of rGO/CNT composite structure.[30–34] The conductive CNT interconnects the adjacent rGO sheets, inducing a well-linked solid-state electrode. The ionic conductivity is hence enhanced. However, the rGO/CNT electrodes in these literature are limited to simple shapes.[30–34] Due to the limited manufacturing capability, the growing demand for SCs with multiplex geometries, exquisite constructions, and advanced functions underscores the need for advanced manufacturing technologies that can quickly fabricate arbitrary complicated rGO/CNT electrode structures. Direct ink writing (DIW) is a syringe extrusion-based 3D printing technique. Next-generation electronics made by DIW method are demonstrating several unique features including customizability and a wide range of materials.[35–40] Herein, we investigate the DIW process for fabricating the proposed SCs with SMA and rGO/CNT inks.

In this study, we investigate direct digital manufacturing of wearable thermoresponsive supercapacitor, through the preparation of rGO/CNT composite ink and development of a novel elevated-temperature DIW process to print hybrid rGO/CNT electrodes and LiCl electrolyte on SMA substrates. In the rGO/CNT composite electrodes, the CNTs serve as a spacer between the graphene to give rise to rapid diffusion pathways for the electrolyte ions. CNTs also serve as a binder to hold the graphene together, preventing the disintegration of the graphene structure into the electrolyte. Additionally, to preserve SCs temperature-dependent shape-changing property and improve SCs reliability, our proposed DIW process prints elastomer layers to seal the whole SCs structure fully, and hence fabricate entirely packaged thermoresponsive SCs in one-platform and one-job without any assembly or postprocessing steps. Several manufacturing-related parameters, such as time-dependent printing speed and curing temperature for both elastomer and rGO/CNT ink, are investigated to fabricate this integrated design.

To fabricate an SC, flexible housing for the thermoresponsive SMA plate is first printed at an elevated temperature. The design of the highly flexible, lightweight, nonbiodegradable housing is inspired by a leaf-like architecture (**Figure 1**a,e). The flexibility not only accommodates the SMA bending and flattening but also provides robust protection to the human body for wearable applications. The SMA plate, which is entirely covered with a stretchable film mask, is placed in the housing (Figure 1b). The rGO/CNT ink is then deposited repeatedly in a layer-by-layer fashion onto the film substrate, using a DIW technique. The DIW system setup is shown in the supporting information (Figure S1, Supporting Information). Herein, to demonstrate the capability of manufacturing complicated geometries, a Hilbert-pattern in-plane supercapacitor design is investigated (Figure 1c,f). The pattern is inspired by conventional supercapacitor interdigital structures, which are suitable for both sensing and wearable energy storage device applications (The dimensions are shown in Figure S2 in the Supporting Information).[41,42] The DIW printing resolution of carbon-based materials in recently reported literature is in the range of 0.5–2.0 mm.[44,45] To maintain the maximum pristine carbon material properties for high energy performance, many carbon material based inks used in the DIW process are free of binders, which results in poor dispersion of carbon-based materials in a watery mixture.[43,48] The rheological issue of those low-viscosity inks limits the printing resolution in the DIW process. It is also more likely to cause tip clogging issue due to the carbon-based material agglomeration. In comparison, the printing resolution of the electrodes in this study is characterized to be 175 ± 25 μm, which is among the best in the recently reported planar carbon-based energy storage devices fabricated by DIW technique.[44,45] The superior printability is beneficial from strong shear-thinning behaviors and moderate viscosities of the inks prepared in this study. The shear-thinning property of our rGO/CNT ink allows a stable extrusion from the dispensing tip without clogging, and its moderate viscosity provides an equilibrium contact angle in the range of

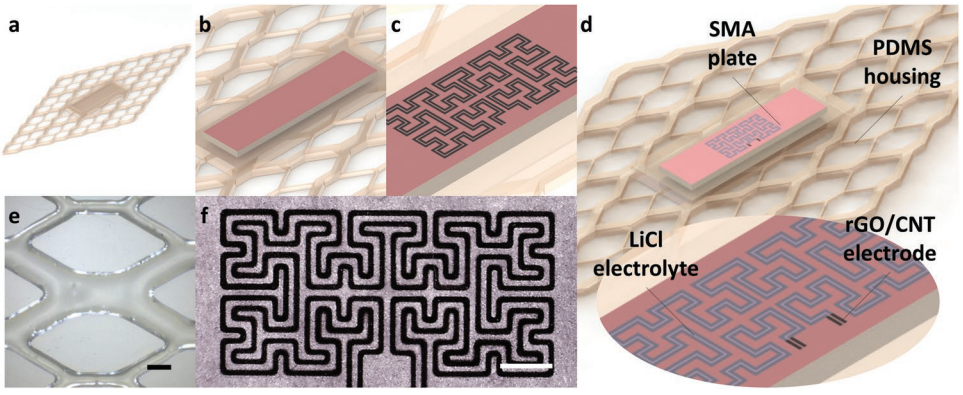

Figure 1. SC design. a) Schematic drawing of elastomer housing. b) Schematic drawing of SMA plate. c) Schematic drawing of rGO/CNT electrodes. d) Schematic drawing of the integrated SC design. e) Printed elastomer housing (scale bar = 1 mm). f) Printed rGO/CNT electrodes (scale bar = 2 mm).

50–70°, which makes it possible to fabricate fine features using DIW. After evaporating water contents in the printed rGO/CNT layer, acids are printed on the dried rGO/CNT layer, to remove the impurities and surfactants remained in it.[45] The acids are deposited in a dot-by-dot way, instead of a continuous trace, to avoid the common bulge problem due to its low viscosity (1.2 mPa s at room temperature).[46,47] Afterward, acetone and deionized water are used to neutralize the printed electrodes. The electrodes are further connected by writing aqueous LiCl electrolyte onto the pattern (Figure 1d). The fabrication is completed upon the printing of an elastomer layer on the top of the electrolyte to adequately package the SCs to improve the reliability in the long term. A detailed description of material preparation is provided at the end of this paper. Besides, the printing process settings for varied inks are described in detail in the Supporting Information.

In this study, the material for printing the housing is a polydimethylsiloxane (PDMS)-based elastomer (SYLGARD 184 Silicone). It is a two-part (base and curing agent, 10:1 mixing ratio), clear, room temperature and heat cured elastomer with ≈90 min pot life. After this 90-minute pot life, the material viscosity would be significantly changed due to the crosslinking. The curing time for the elastomer at 100 °C is 35 min according to the specification. The printing usually requires 5 to 15 layers to print the PDMS housing structure with a height of 1.2 mm to house the SMA plate properly, depending on the layer thickness which could be in the range of 0.1–0.3 mm. Before a new layer deposition, the previous layer needs to be heated for 30 min to solidify fully. Therefore, the printing time can range from 2 to 6 h, which is longer than the material pot life, making the printing process challenging or even impossible. To address this challenge, we investigated the viscosity dynamics of the elastomer and the corresponding printing process settings.

Figure 2a shows the viscosity change of the elastomer within the first 6 h after mixing base and curing agent. The measured apparent viscosity at a consistent 0.1 s^{-1} shear rate increases from 3.0 to 8.9 Pa s. The elastomer is extruded using a 0.46 mm inner diameter blunt dispensing tip (5.0 psi air pressure) at a 10 mm s^{-1} printing velocity into 20 mm traces to investigate the influence of the gradually increased viscosity to the printed geometry (trace width). The measured trace width decreases from 1180 to 501 μm within the first 6 h after mixing. As a result, with the conventional uniform printing speed, the printed multilayer structure will have significant shrinkages along the printed trace width direction, which will further result in printing defects such as air gaps between traces within the layer and geometry inaccuracy.

The printed geometric change can be explained by the printed trace dimension model shown in Equation (1): the printed trace width W and height H are functions of printing velocity v, flow rate Q, and the ink equilibrium contact angle θ[47]

$$\begin{cases} W = \sqrt{\dfrac{4Q}{v\left(\dfrac{\theta}{sin^2(\theta)} - \dfrac{\cos(\theta)}{\sin(\theta)}\right)}} \\ H = \dfrac{W}{2}\left(\dfrac{1}{sin\theta} - \dfrac{1}{tan\theta}\right) \end{cases} \quad (1)$$

It should be noted that the flow rate is dependent on the ink viscosity.[43] Therefore, to address the shrinkage problem during PDMS printing, a possible solution is to adjust the printing velocity over time, as illustrated in Figure 2b. Also, because the chemical properties of the PDMS ink are changing during the printing process, the curing temperature should be adjusted appropriately. Samples with a 20 mm by 10 mm rectangular shape are printed and heated at 75, 100, and 125 °C substrate, respectively (Figure 2c), to identify the appropriate curing temperature at different printing time. Although samples solidified at 75 °C shows smooth surface, the boundaries are blurred, and the curing time (>60 min) is over-long for multilayer DIW process, considering the relatively short pot life of the elastomer ink. Samples solidified at 125 °C show separated traces due to the over-fast curing, which leaves little time for traces to merge to form an integral and smooth surface properly. Several undesired pores are also observed at the printed trace corner while samples printed at 100 °C show clear boundaries and smooth surface.

To print the Hilbert electrode pattern, the rGO/CNT composite ink is deposited repeatedly onto a heated substrate in a layer-by-layer way (25 layers in total). After the deposition of a new layer, it is thoroughly dried by the heated substrate, as demonstrated in Figure 2d. It should be noted that the first layer of rGO/CNT is printed onto a stretchable film substrate, while the remaining layers are printed onto the previously dried rGO/CNT. To investigate the influence of both substrates on the printed trace geometry, rGO/CNT (CNT-10%, the ink info. is provided in experimental section) ink is extruded through a 0.96 mm inner diameter dispensing tip onto the stretchable film substrate and the dried rGO/CNT substrate, separately. As shown in Figure 2e, the solidified trace width decreases from 1.92 to 1.51 mm. Such geometry change is mainly caused by the wettability of both substrates, which is also confirmed by the equilibrium contact angle measurement shown in Figure 2f. Stretchable film (51.1°) shows a higher wettability than the dried rGO/CNT (75.5°) substrate. Hence, to compensate for the effects of two different substrates for a consistent trace width, the printing velocities are adjusted based on the measurements. In addition to tuning the printing velocity for printing on varied substrates, the heating temperature for rGO/CNT ink is also adjusted. Herein, a single-layer 10 mm by 10 mm structure is printed onto a glass substrate and heated at 75, 100, 150, and 200 °C until thoroughly dried, respectively. Although higher temperature can rapidly solidify the printed ink, it leaves considerate pores onto the dried surface. In this study, D_{max} is defined as the maximum observed pore diameter under a microscope. Figure 2g shows the optical images of samples heated at different temperatures. Samples heated at 75 °C shows little pores (D_{max} at 75 °C = 134 μm). The observed maximum pore diameter is increased by increasing heating temperature (D_{max} at 100 °C = 258 μm, D_{max} at 150 °C = 431 μm, D_{max} at 200 °C = 495 μm).

The thermoresponsive mechanism of the typical in-plane SC design is characterized by the SMA bending angle θ and the cell geometries (electrode length L, width W, and the distance D between two electrodes in millimeter, **Figure 3**a). In general, θ is a function of temperature T, ranging from 20 to 60 °C in wearable applications

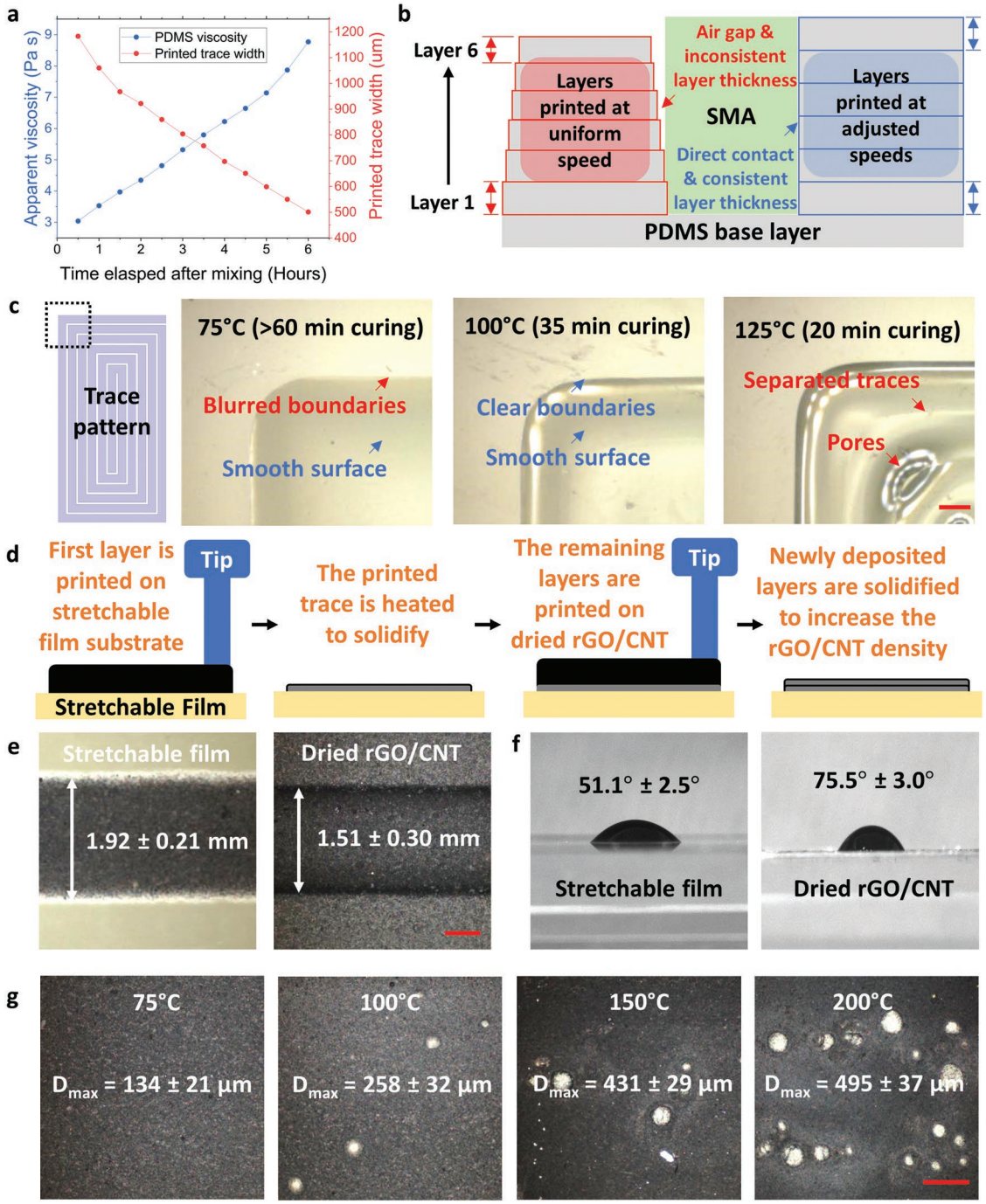

Figure 2. DIW process investigation. a) Apparent viscosity and printed trace width influenced by the time elapsed after elastomer base and curing agent mixing. b) Demonstration of the non-adjusting speed and adjusting speed methods for layer-by-layer elastomer printing. c) Elastomer curing temperature investigation for optimizing printed surface quality of a single layer, 20 mm by 10 mm by 20 mm rectangular samples (scale bar = 0.5 mm). d) Step-by-step illustration of the layer-by-layer printing process of rGO/CNT electrodes on a heated substrate. e) Trace width comparison between samples printed onto stretchable film and dried rGO/CNT substrates under the same setting (scale bar = 0.5 mm). f) Equilibrium contact angle measurements of rGO/CNT ink on stretchable film and dried rGO/CNT substrates. g) Observation of undesired pores on dried single-layer rGO/CNT sample surface at different heating conditions (scale bar = 1 mm).

$$\theta = f(T) \tag{2}$$

To further estimate the capacitance of thermoresponsive SCs, we assume the active materials are uniformly distributed with a planar density α (mg mm^{-2}), and the pore surface is entirely fulfilled by the electrolyte. The capacitance C (mF) of the typical in-plane SC design given a bending angle θ is approximated by

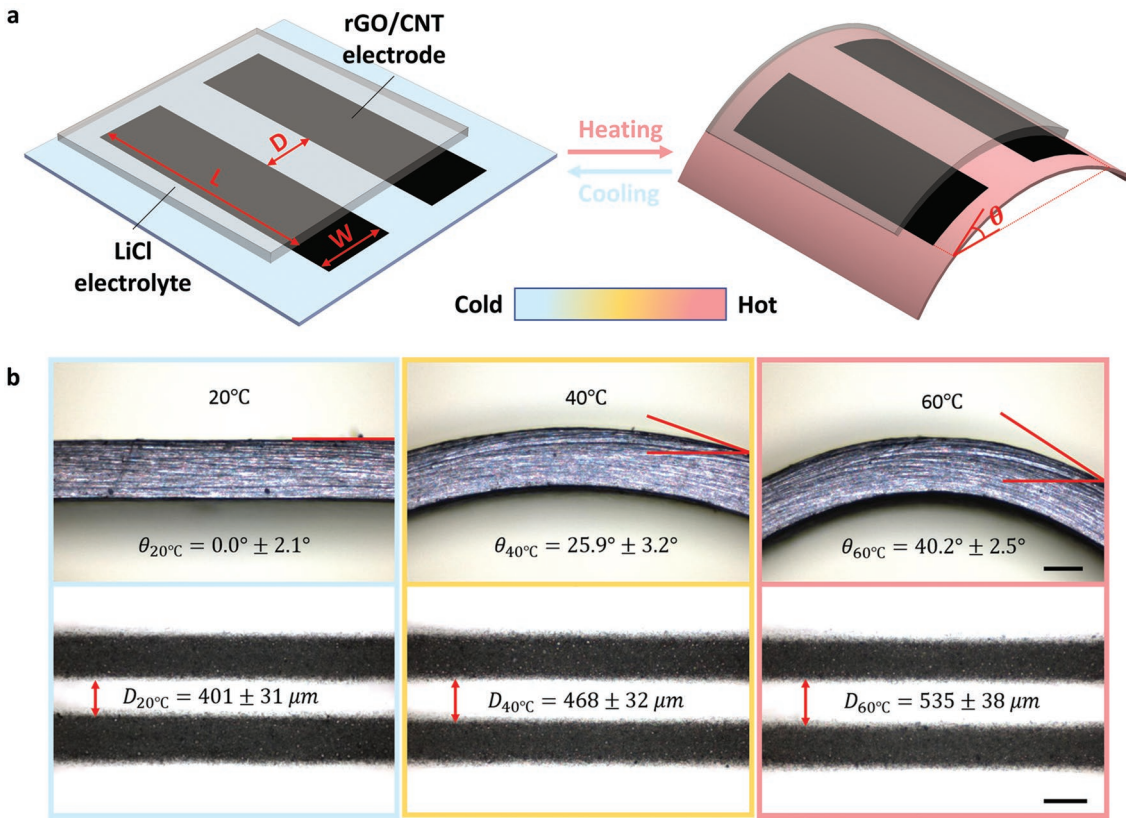

Figure 3. Thermoresponsive mechanism illustration. a) Schematic drawing of typical in-plane SC under temperature change. b) Measured thermoresponsive geometry dynamics of the as-fabricated single SC cell (side view scale bar = 0.2 mm, top view scale bar = 0.5 mm).

$$C = \frac{\varepsilon\alpha\beta WL\,sinc\theta}{D+W} \tag{3}$$

where ε is the permittivity, and β ($m^2\ mg^{-1}$) is the surface area of the active materials. Substituting Equation (2) to Equation (3), we obtain

$$C = \frac{\varepsilon\alpha\beta WL\,sin\left[f(T)\right]}{(D+W)\,f(T)} \tag{4}$$

When the surrounding temperature of an SMA increases from T_1 to T_2, the corresponding bending angle varies from θ_1 to θ_2. The capacitance difference ΔC caused by the thermal change is

$$\Delta C = \frac{\varepsilon\alpha\beta WL}{(D+W)}\left[\frac{\sin\theta_1}{\theta_1} - \frac{\sin\theta_2}{\theta_2}\right] = \frac{\varepsilon\alpha\beta WL}{(D+W)}\left\{\frac{\sin[f(T_1)]}{\sin(T_1)} - \frac{\sin[f(T_2)]}{\sin(T_2)}\right\} \tag{5}$$

According to the current–voltage relation of typical capacitors, the current density reduction percentage p_1 is

$$p_1 = \frac{\Delta C}{C} = 1 - \frac{\theta_1 sin\theta_2}{\theta_2 sin\theta_1} = 1 - \frac{f(T_1)\sin\left[f(T_2)\right]}{f(T_2)\sin\left[f(T_1)\right]} \tag{6}$$

Based on the Joule heating equation, the deformation-caused heat reduction percentage p_2 in a current path for preventing thermal runaway is

$$p_2 = p_1^2 \tag{7}$$

In this study, the bending angles of a 12.0 mm by 6.0 mm SMA plate patterned with a typical in-plane SC cell (W = 0.5 mm, L = 5.0 mm, D = 0.4 mm at 20 °C) are measured under various temperatures (Figure 3b). As calculated, if the SC endures a thermal change from 20 to 60 °C possibly due to improper long-term use or harsh environments, the heat produced by excessive current or other overheated components is alleviated ≈35% by the proposed design.

Studies have shown that pure rGO has a stacked structure with local folding and non-uniform stacking.[41] Such heavily stacked rGO sheets hinder the fast transportation of electrolyte ions to the pore surface. The hybrid rGO/CNT electrodes exhibit higher energy densities, implying the use of CNTs as a spacer between rGO sheets is an efficient approach to enlarge the electrode accessible surface area. In this study, a homogeneous aqueous solution of rGO and CNT composite is used for DIW deposition on preheated (85 °C) substrates. To identify the proper preparation of rGO/CNT composite ink, samples labeled as CNT-10%, CNT-25%, and CNT-50% were tested with rGO and CNT weight ratios of 9:1, 3:1, and 1:1, respectively. The thicknesses of thoroughly dried printed electrodes are ≈6 µm for each ink. Figure S3 in the Supporting Information demonstrates the scanning electron microscopy (SEM) images of the printed CNT-25% electrodes. A uniformly packed film with CNTs scattered between rGO sheets is observed, which efficiently alleviates the pristine rGO stacking.

In addition, to study the influence of the ink ratio on the electrochemical performance, we fabricated sandwiched SCs with 15 mm by 2.5 mm electrodes (175 µm gap between electrodes) and tested their performance in aqueous LiCl electrolytes by using cyclic voltammetry (CV) and galvanostatic methods with a potential range from 0 to 1 V (**Figure 4**a,b). During the initial CV cycles, at 100 mV s^{-1} scan rate, the measured cycling current remained within a roughly equivalent level, indicating the absence of the electro-activation.[42,49] It implies that the intercalation of CNTs in the printed rGO/CNT ink effectively alleviates rGO sheet restacking. On the other hand, the CV tests indicate that the CNT-25% ink exhibits a superior power handling capability than CNT-10% and CNT-50%. Such observations are also verified by the results from the galvanostatic test at 50 mA cm^{-3}. The performance characterization using other settings and detailed procedures for the device preparation is described in Figure S4 in the Supporting Information. The specific capacitances at various current densities are summarized in Figure 4c. To study the thermal dynamic of the proposed rGO/CNT composite in the aqueous LiCl system, we tested the sandwiched SC (CNT-25%) under varied thermal conditions from 20 to 60 °C. The galvanostatic charge/discharge profiles at 50 mA cm^{-3} rate from 0 to 1 V under varied thermal conditions (20 to 60 °C) are shown in Figure S5 in the Supporting Information. The electrochemical performance results indicated that this SC architecture is barely affected by the temperature change from 20 to 60 °C on a non-thermoresponsive substrate. The corresponding EIS measurements of SC in terms of temperature (Figure S6, Supporting Information) also confirms the minimal variation of the electrochemical temperature coefficient in this temperature range.[50]

The resistivity of thoroughly dried electrodes is measured from 6 µm printed films (Figure 4d), which is adequate for the formation of a conductive thin film. After nitric acid treatment, the resistivity is dramatically reduced by removing surfactants and impurities. To study the influence of the thermal conditions on the electrode conductivity, the resistivity from acid-treated rGO/CNT ink (CNT-25%, 15 mm by 2.5 mm electrodes, 6 µm thick) was measured under varied thermal conditions, the results were plotted in Figure S7 in the Supporting Information. The conductivity was found to slightly decreases (<5%) when the temperature increases from 20 to 60 °C, which is consistent to related study about the conductivity of carbon-based low-dimensional materials.[51] The slight variations of the rGO/CNT electrode conductivity indicate the minor influence caused by the temperature range from 20 to 60 °C on the electrode performance in a non-thermoresponsive architecture. The ionic conductivity of the electrolyte under varied thermal conditions was estimated according to the EIS characterization (Figure S6, Supporting Information), the calculated results were included in Supporting Information. The aqueous electrolyte solution showed close ionic conductivities (from 1.2 to 1.4 $m\Omega^{-1}$ cm^{-1}) in this temperature range. The results revealed that the influence of temperature to the ion conductivity of the LiCl electrolyte is insignificant.

The apparent viscosity of the three inks is characterized (Figure 4e). They demonstrate a similar intense shearing thinning behavior, which ensures a stable and consistent printing

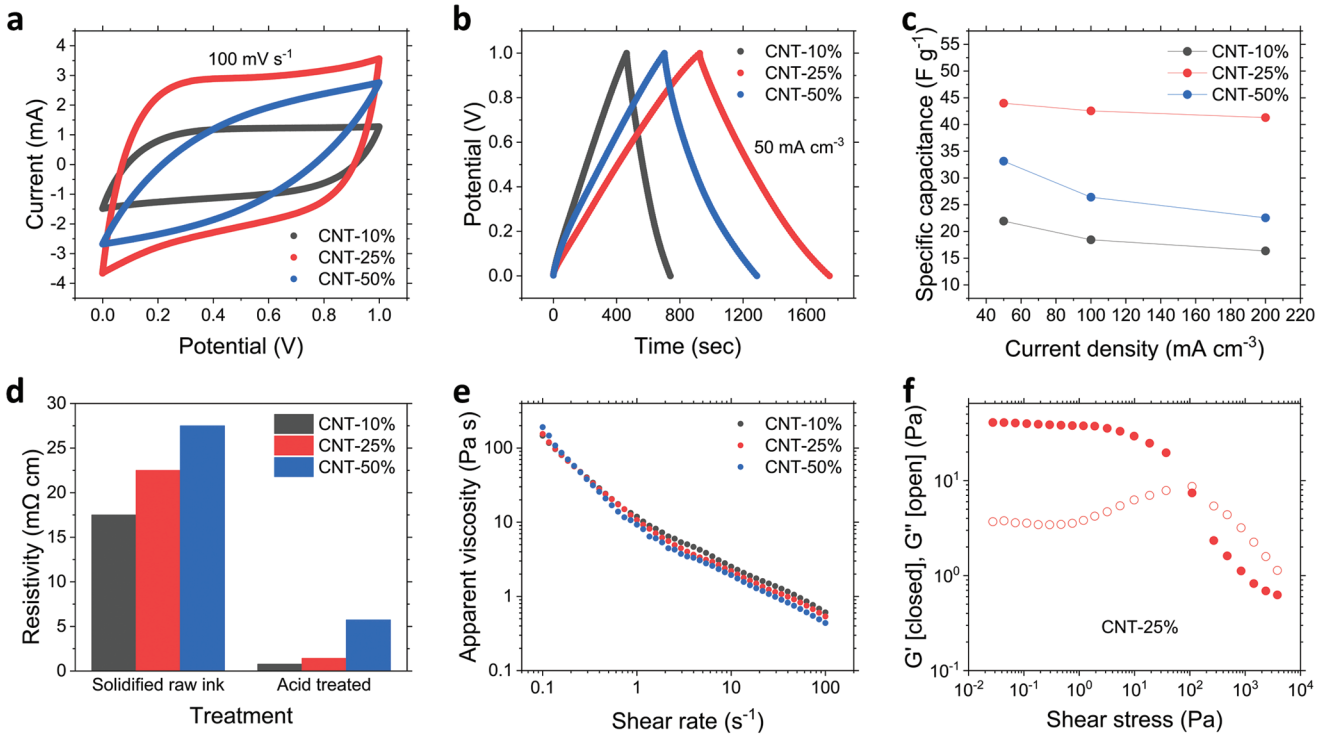

Figure 4. Characterizations of electrodes from CNT-10%, CNT-25%, and CNT-50% inks. a) CV profiles. b) Galvanostatic charge/discharge profiles. c) Specific capacitance at various current densities. d) Resistivity measurements. e) Apparent viscosity measurements. f) Storage modulus and loss modulus measurements.

process of DIW. The measured apparent viscosities mainly decrease from 106.5 to 0.5 Pa s when the shear rate varies from 0.1 to 100 s^{-1}. Figure 4f shows the storage modulus (G′) and loss modulus (G″) as a function of shear stress for CNT-25% ink. It is an elastic-like solid (G′ ≫ G″) with respective G′ values of 40.9 Pa that flows when its shear yield stress value of 109.68 Pa is exceeded. Once the ink exits the nozzle and returns to a zero-shear condition, it rapidly solidifies and retains their filamentary shape. CNT-10% and CNT-50% inks showed similar rheological behaviors. The corresponding measured G′ and G″ are demonstrated in Figure S8 in the Supporting Information. The trace width printed at 3.0 psi through a 100 µm inner diameter tip at various speed is characterized (Figure S9, Supporting Information). By varying the print speed, the printed features produced from three inks can be adjusted. The contact angle characterization of three ink is included in Figure S10 in the Supporting Information.

Herein, an external heating source is employed to mimic the thermal runaway situation to demonstrate the effective thermoresponsive self-protection mechanism of fabricated SCs. The electrodes are fabricated by extruding CNT-25% ink in a Hilbert pattern where aqueous LiCl serves as the electrolyte. The entire SC is sealed and protected by the printed elastomer. The temperature-dependent CV curves at 50 mV s^{-1} scan rate of shape memory alloy integrated SCs are shown in **Figure 5**a. Upon increasing the temperature from 20 to 60 °C, the charge–discharge currents decrease to avoid burst heat generation. Similar trends are also observed from the galvanostatic test at 20 mA cm^{-3} (Figure 5b). This indicates the printed SC functionalize appropriately in a wide temperature range due to the integrated SMA substrates. The performance characterization using other settings is also described in Figure S11 in the Supporting Information. The specific capacitances at various current densities are summarized in Figure 5c. The specific capacitance of printed SCs at different current densities decreases by increasing the ambient temperature. Such reduction suggests that the temperature-dependent electrode geometry enables dynamic responses in the specific capacitance of SCs. According to Equations (6) and (7), the estimated heat reduction percentage is ≈40%. When thermal runaway happens by increased ambient temperature, it weakens the power delivery dynamically by inhibiting the transportation of conductive ions to prevent potential damages.

To further investigate the inhibition of the ion transportation by the functional thermal responsive design, the impedance of SCs is measured through electrochemical impedance spectroscopy (EIS) approach (Figure 5d). In general, the impedance of an SC is mainly determined by two distinct processes: the charge transfer during a fast voltage change at the electrode-electrolyte interface (high frequency), as well as the ion diffusion during a slow voltage change within the electrolyte (low frequency). In this study, the temperature-dependent SC structure design enables a dynamic impedance at low frequency. For typical in-plane SC designs, the electrolyte resistance is affected by the resistivity of the electrolyte and cell constant. A larger electrode gap leads to a higher electrolyte resistance, degrading capacitive performance. The equivalent series resistance (ESR) of the printed SC increases from 85 to 160 Ω when

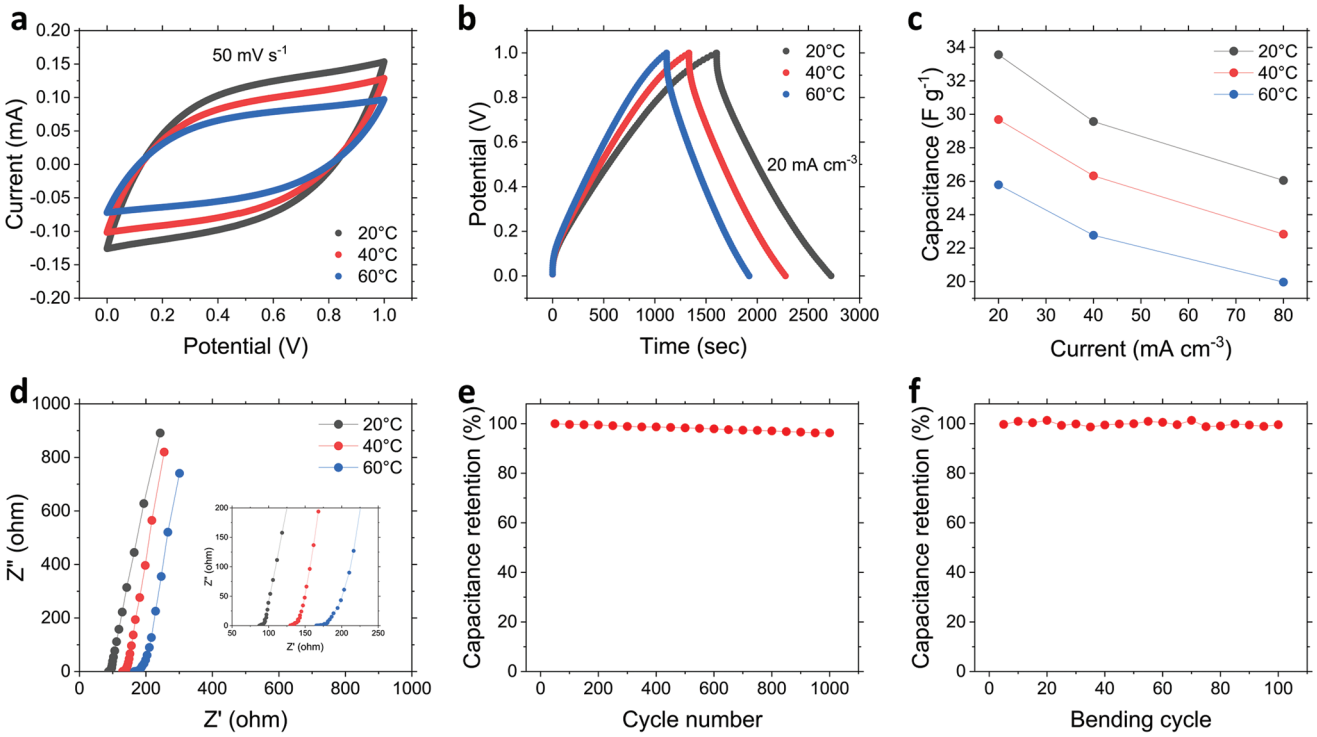

Figure 5. Illustrations of thermoresponsive supercapacitor from 20 to 60 °C. a) CV profiles. b) Galvanostatic charge/discharge profiles. c) Specific capacitance at various current densities. d) Nyquist plot from EIS. e) Capacitance retention of 1000 cycles under a current density of 80 mA cm^{-3} at 20 °C. f) Capacitance retention at different bending cycles.

the temperature is rising from 20 to 60 °C, mainly caused by the increased electrode resistance. The increased ESR results in a drop of voltage during the charge/discharge process, which reduces the usable capacity of the SC. These results verified that the impedance of the SC is highly temperature-dependent, providing self-protection against the thermal runaway. Compared with conventional passive approaches to solving thermal runaway in energy storage devices, our proposed strategy employs a reversible active self-protection mechanism. Besides, the printed SC is found to be robust under temperature changes, demonstrating a 95.6% retention after 1000 cycles at a current density of 80 mA cm^{-3} (Figure 5e) and retains its original capacitance after 100 bending cycles (Figure 5f). The comparison between this work and other recently reported thermoresponsive energy storage device related studies are summarized in the Supporting Information (Table S1, Supporting Information).[52–55] Our work is one of the very few studies reporting the complicated geometry, high fabrication resolution, integrated design, competitive energy storage performance, and sensitive and reliable thermoresponsive dynamics.

In summary, we have demonstrated a thermoresponsive SC design and fabrication strategy for self-protective wearable SCs devices via a novel elevated-temperature direct ink writing process. Manufacturing-related parameters such as time-dependent printing speed and curing temperature are investigated. The printed SC consists of patterned electrodes as thin as 175 μm and flexible silicone housing. The proposed temperature-dependent structure provides an as high as 8 F g^{-1} automatic adjustment in specific capacitance, resulting in an overall heat reduction up to 40%. The optimal composition of rGO and CNT in the composite ink are characterized. The thermoresponsive mechanism enables the dynamic charge–discharge rate capability under various temperature, leading to an active and reversible constraint of the thermal runaway. This study shows tremendous promise for future intelligent power delivery applications such as wearable energy storage devices and smart self-charged thermal sensing and actuating devices.

Experimental Section

Preparation of Electrolyte Ink (LiCl): The electrolyte was prepared by adding lithium chloride powder (12 g, >99.0%, Sigma-Aldrich) to deionized water (40 mL), followed by stirring (Eurostar 60, IKA) for 5 min at a 500 rpm rotating speed before storing at room temperature.

Preparation of rGO and CNT Composite Electrode Ink (rGO/CNT): First, 2 mg mL^{-1} rGO and CNT aqueous solution were prepared separately. Large surface area SWNT (purity > 95%, specific surface area > 1075 m^2 g^{-1}) was purchased from Timesnano (product code TNSAR, Chengdu, China) and used as received. CNT (100 mg) and sodium dodecyl sulfate powder (350 mg, >99.0%, Sigma-Aldrich) were added into deionized water (50 mL). Reduced Graphene Oxide (BET surface area: 422.69–499.85 m^2 g^{-1}) was purchased from Graphenea (product code rGO, Spain) and used as received. rGO (100 mg) and sodium dodecyl sulfate powder (350 mg) were added into deionized water (50 mL). Then, both solutions were mixed (AR-100, Thinky) at 2000 rpm for 15 min, followed by 1-hour probe sonication (QSonica Q500, 70% power) to uniformly disperse active materials in the rGO solution and CNT solution, separately. According to the desired ratio, a total volume 2 mL rGO and CNT solution, together with 0.8 mL Cellink Start (Cellink, Sweden) were mixed at 2000 rpm for 3 min before loading to a 10 cc syringe barrel attached to the direct ink writing setup.

Preparation of the Ink for Silicone Housing (Elastomer): Dow Sylgard 184 silicone elastomer was purchased and used as received. It was a two-component (mix ratio 10:1), room temperature curing encapsulant that was used as a protective coating for electronics. In this study, two components were first mixed at 2000 rpm for 5 min before loading to a 10 cc syringe barrel. After fully sealing the printed in-plane SC, it was solidified at 25 °C for 48 h.

Preparation of Two-Way Shape Memory Alloy Plates (SMAP): The shape memory alloy plates (140 mm by 6 mm by 0.3 mm) were purchased from Baoji Seabird Metal Material Co (China). It was then carefully cut and polished into 12.0 mm by 6.0 mm by 0.3 mm pieces. The as-cut plate was flat at 15 °C. It starts to curve when the temperature increases and reaches the maximum curvature until stabilizing at 65 °C. It recovers to the flattened shape when the environment temperature decreases to 15 °C. A stretchable film (Scotch 8884) was then attached to the SMAP.

Rheological Measurements: In this study, the rheological properties were measured by a rotational rheometer (Kinexus ultra+, Malvern) under a 25 mm diameter plate geometry. The plate geometry was supported by a virtually frictionless air-bearing and driven by an ultralow inertia motor, coupled to an ultrahigh precision position encoder. The inks were stabilized at 25 °C for 15 min before loading into the 0.3 mm gap between the fixed substrate and the movable plate geometry. The rheological properties were characterized by the controllable motor torque. The test usually runs a logarithmic sequence of shear rates while measuring the apparent viscosity at 25 °C for each material.

Electrochemical Measurements: All the printed cells were tested using a Bio-Logic VMP3 Potentiostat electrochemical workstation. The environmental temperature was controlled by a temperature test chamber (Binder FP53, Germany). The Galvanostatic charge/discharge of the cells was tested at a scanning rate ranging from 20 to 200 mA s^{-1}. The electrochemical impedance spectroscopy test results were collected in a frequency range of 0.1 Hz–1 MHz.

Supporting Information

Supporting Information is available from the Wiley Online Library or from the author.

Acknowledgements

This project was partially supported by National Science Foundation (NSF) Grant 1825626. M.C. and R.S.-Y. were supported by NSF award CBET-1805938. The authors are thankful to the support from NSF and the support from the Battery Cluster in UIC College of Engineering and the Electron Microscopy Service from the UIC Research Resources Center. The authors thank David Mecha of the Engineering Machine Shop for assistance with SMA sample preparation.

Conflict of Interest

The authors declare no conflict of interest.

Keywords

direct ink writing, rGO/CNT composites, shape memory materials, thermoresponsive supercapacitors, wearable electronics

Received: August 12, 2019
Revised: September 11, 2019
Published online: October 18, 2019

[1] A. Yu, I. Roes, A. Davies, Z. Chen, *Appl. Phys. Lett.* **2010**, *96*, 253105.
[2] L. Hu, H. Wu, Y. Cui, *Appl. Phys. Lett.* **2010**, *96*, 183502.
[3] P. Chen, G. Shen, S. Sukcharoenchoke, C. Zhou, *Appl. Phys. Lett.* **2009**, *94*, 043113.
[4] C. Yu, C. Masarapu, J. Rong, B. Wei, H. Jiang, *Adv. Mater.* **2009**, *21*, 4793.
[5] X. Feng, J. Sun, M. Ouyang, F. Wang, X. He, L. Lu, H. Peng, *J. Power Sources* **2015**, *275*, 261.
[6] Q. Wang, P. Ping, X. Zhao, G. Chu, J. Sun, C. Chen, *J. Power Sources* **2012**, *208*, 210.
[7] A. Hofmann, N. Uhlmann, C. Ziebert, O. Wiegand, A. Schmidt, T. Hanemann, *Appl. Therm. Eng.* **2017**, *124*, 539.
[8] A. Hammami, N. Raymond, M. Armand, *Nature* **2003**, *424*, 635.
[9] S. C. Mukhopadhyay, *IEEE Sens. J.* **2015**, *15*, 1321.
[10] M. Stoppa, A. Chiolerio, *Sensors* **2014**, *14*, 11957.
[11] W. Zeng, L. Shu, Q. Li, S. Chen, F. Wang, X. Tao, *Adv. Mater.* **2014**, *26*, 5310.
[12] K. Jost, D. Stenger, C. R. Perez, J. K. McDonough, K. Lian, Y. Gogotsi, G. Dion, *Energy Environ. Sci.* **2013**, *6*, 2698.
[13] S. Lee, S. Shin, S. Lee, J. Seo, J. Lee, S. Son, H. J. Cho, H. Algadi, S. Al-Sayari, D. E. Kim, *Adv. Funct. Mater.* **2015**, *25*, 3114.
[14] J. Lee, H. Kwon, J. Seo, S. Shin, J. H. Koo, C. Pang, S. Son, J. H. Kim, Y. H. Jang, D. E. Kim, *Adv. Mater.* **2015**, *27*, 2433.
[15] L. Kou, T. Huang, B. Zheng, Y. Han, X. Zhao, K. Gopalsamy, H. Sun, C. Gao, *Nat. Commun.* **2014**, *5*, 3754.
[16] X. Pu, L. Li, H. Song, C. Du, Z. Zhao, C. Jiang, G. Cao, W. Hu, Z. L. Wang, *Adv. Mater.* **2015**, *27*, 2472.
[17] M. Osman, M. A. Rahim, N. A. Samsuri, H. A. M. Salim, M. F. Ali, *Prog. Electromagn. Res.* **2011**, *117*, 321.
[18] U. Anliker, J. A. Ward, P. Lukowicz, G. Troster, F. Dolveck, M. Baer, F. Keita, E. B. Schenker, F. Catarsi, L. Coluccini, A. Belardinelli, D. Shklarski, M. Alon, E. Hirt, R. Schmid, M. Vuskovic, *IEEE Trans. Inf. Technol. Biomed.* **2004**, *8*, 415.
[19] D. Raskovic, T. Martin, E. Jovanov, *Comput. J.* **2004**, *47*, 495.
[20] G. Song, N. Ma, H. Li, *Eng. Struct.* **2006**, *28*, 1266.
[21] L. Machado, M. Savi, *Braz. J. Med. Biol. Res.* **2003**, *36*, 683.
[22] D. J. Hartl, D. C. Lagoudas, *Proc. Inst. Mech. Eng., Part G* **2007**, *221*, 535.
[23] Q. Ge, H. J. Qi, M. L. Dunn, *Appl. Phys. Lett.* **2013**, *103*, 131901.
[24] Q. Ge, C. K. Dunn, H. J. Qi, M. L. Dunn, *Smart Mater. Struct.* **2014**, *23*, 094007.
[25] L. Huang, R. Jiang, J. Wu, J. Song, H. Bai, B. Li, Q. Zhao, T. Xie, *Adv. Mater.* **2017**, *29*, 1605390.
[26] Q. Ge, A. H. Sakhaei, H. Lee, C. K. Dunn, N. X. Fang, M. L. Dunn, *Sci. Rep.* **2016**, *6*, 31110.
[27] M. Zarek, M. Layani, I. Cooperstein, E. Sachyani, D. Cohn, S. Magdassi, *Adv. Mater.* **2016**, *28*, 4449.
[28] C. Niu, E. K. Sichel, R. Hoch, D. Moy, H. Tennent, *Appl. Phys. Lett.* **1997**, *70*, 1480.
[29] Y. Zhu, S. Murali, W. Cai, X. Li, J. W. Suk, J. R. Potts, R. S. Ruoff, *Adv. Mater.* **2010**, *22*, 3906.
[30] S. Woo, Y. Kim, T. D. Chung, Y. Piao, H. Kim, *Electrochim. Acta* **2012**, *59*, 509.
[31] Q. Cheng, J. Tang, J. Ma, H. Zhang, N. Shinya, L. Qin, *Phys. Chem. Chem. Phys.* **2011**, *13*, 17615.
[32] D. Zhang, T. Yan, L. Shi, Z. Peng, X. Wen, J. Zhang, *J. Mater. Chem.* **2012**, *22*, 14696.
[33] S. Stankovich, D. A. Dikin, G. H. Dommett, K. M. Kohlhaas, E. J. Zimney, E. A. Stach, R. D. Piner, S. T. Nguyen, R. S. Ruoff, *Nature* **2006**, *442*, 282.
[34] H. Sun, X. You, J. Deng, X. Chen, Z. Yang, J. Ren, H. Peng, *Adv. Mater.* **2014**, *26*, 2868.
[35] A. D. Valentine, T. A. Busbee, J. W. Boley, J. R. Raney, A. Chortos, A. Kotikian, J. D. Berrigan, M. F. Durstock, J. A. Lewis, *Adv. Mater.* **2017**, *29*, 1703817.
[36] T. Wei, B. Y. Ahn, J. Grotto, J. A. Lewis, *Adv. Mater.* **2018**, *30*, 1703027.
[37] M. A. Skylar-Scott, S. Gunasekaran, J. A. Lewis, *Proc. Natl. Acad. Sci. USA* **2016**, *113*, 6137.
[38] J. A. Lewis, J. E. Smay, J. Stuecker, J. Cesarano, *J. Am. Ceram. Soc.* **2006**, *89*, 3599.
[39] M. Wehner, R. L. Truby, D. J. Fitzgerald, B. Mosadegh, G. M. Whitesides, J. A. Lewis, R. J. Wood, *Nature* **2016**, *536*, 451.
[40] N. Zhou, C. Liu, J. A. Lewis, D. Ham, *Adv. Mater.* **2017**, *29*, 1605198.
[41] D. Zhang, B. Chi, B. Li, Z. Gao, Y. Du, J. Guo, J. Wei, *Synth. Met.* **2016**, *217*, 79.
[42] D. Pech, M. Brunet, P. L. Taberna, P. Simon, N. Fabre, F. Mesnilgrente, V. Conédéra, H. Durou, *J. Power Sources* **2010**, *195*, 1266.
[43] C. O'Mahony, E. U. Haq, C. Sillien, S. A. Tofail, *Micromachines* **2019**, *10*, 99.
[44] Z. Wang, Q. E. Zhang, S. Long, Y. Luo, P. Yu, Z. Tan, J. Bai, B. Qu, Y. Yang, J. Shi, H. Zhou, *ACS Appl. Mater. Interfaces* **2018**, *10*, 10437.
[45] B. Chen, Y. Jiang, X. Tang, Y. Pan, S. Hu, *ACS Appl. Mater. Interfaces* **2017**, *9*, 28433.
[46] P. C. Duineveld, *J. Fluid Mech.* **2003**, *477*, 175.
[47] Y. Jiang, S. Hu, Y. Pan, *3D Print. Addit. Manuf.* **2018**, *5*, 301.
[48] D. Li, M. B. Müller, S. Gilje, R. B. Kaner, G. G. Wallace, *Nat. Nanotechnol.* **2008**, *3*, 101.
[49] Q. Cheng, J. Tang, J. Ma, H. Zhang, N. Shinya, L. Qin, *Carbon* **2011**, *49*, 2917.
[50] C. Gao, S. W. Lee, Y. Yang, *ACS Energy Lett.* **2017**, *2*, 2326.
[51] T. Ebbesen, H. Lezec, H. Hiura, J. Bennett, H. Ghaemi, T. Thio, *Nature* **1996**, *382*, 54.
[52] W. Ji, B. Jiang, F. Ai, H. Yang, X. Ai, *RSC Adv.* **2015**, *5*, 172.
[53] Y. Shi, H. Ha, A. Al-Sudani, C. J. Ellison, G. Yu, *Adv. Mater.* **2016**, *28*, 7921.
[54] X. Xia, Y. Zhang, D. Chao, Q. Xiong, Z. Fan, X. Tong, J. Tu, H. Zhang, H. J. Fan, *Energy Environ. Sci.* **2015**, *8*, 1559.
[55] Z. Chen, P. Hsu, J. Lopez, Y. Li, J. W. To, N. Liu, C. Wang, S. C. Andrews, J. Liu, Y. Cui, *Nat. Energy* **2016**, *1*, 15009.

